Frictional Resistance Increase Due to Hull Roughness: An Analysis of the Hull Form Parameters Influence

Muhammad Luqman Hakim[1], I Ketut Suastika[2], I Ketut Aria Pria Utama[2], Dian Purnamasari[3], Muryadin Muryadin[3]

An awareness of the drag increase brought on by biofouling's roughness on the ship hull is one technique to cut emissions aboard ship. However, predicting the increased drag on ships poses significant challenges. When predicting the rise in frictional resistance (ΔC_F) brought on by roughness, the hull is considered flat. In fact, ship hulls have a variety of shapes, and it is not certain whether this is a factor influencing the magnitude of the increase in resistance due to roughness. In this article, the effect of the hull's form parameters—L/B (ratio of length per breadth), C_B (coefficient block), and L_{CB} (Length of center buoyancy)—on the increase in frictional resistance brought on by roughness have been investigated. The method used to calculate the ship resistance is Computational Fluid Dynamics (CFD) simulation, complemented by roughness modelling using the wall function approach method. The Design of Experiment (DOE) method has been used to vary the shape of the hull model as a variation of the test specimen in this study. The verification and validation tests have been carried out on the CFD simulation results, where the results have been compared with proven empirical methods. Based on the study results, the value of frictional resistance (C_F) and increased frictional resistance (ΔC_F) of all specimens has shown no significant difference in value, evidenced by the variance values, ranging only 1.57-2.1%. Thus, these results prove that the increase in frictional resistance (ΔC_F) due to roughness is sufficient to assume the ship's hull as a flat plate. The other finding is that roughness can also increase the pressure resistance (ΔC_P), and hull shape parameters also contribute towards changes in the value of ΔC_P.

KEY WORDS

~ Roughness
~ biofouling
~ Computational Fluid Dynamics (CFD)
~ hull Form
~ Design of Experiment (DOE)
~ Ship resistance

[1]Universitas Diponegoro, Faculty of Engineering, Semarang, Indonesia
e-mail: mluqmanhak@lecturer.undip.ac.id
[2] Institut Teknologi Sepuluh Nopember, Faculty of Marine Technology, Surabaya, Indonesia
[3] National Research and Innovation Agency of Indonesia (BRIN), Research Center of Hydrodynamics Technology, Surabaya, Indonesia
doi: 10.7225/toms.v12.n02.002
Received on: <date>; Revised on: 5 Feb 2023, 10 Apr 2023; Accepted on: 18 Jul 2023; Published: 21 Oct 2023

1. INTRODUCTION

One of the significant issues facing the maritime transportation industry is the harmful effects of biofouling roughness. Biofouling adhering to the hull can cause its surface to become rough, potentially increasing frictional resistance (Schultz, 2007). An increase in frictional resistance due to a rough hull surface can require the ship to generate more propeller thrust to maintain speed, resulting in a loss of sailing speed due to the engine's limited power (Hakim *et al.*, 2017). With a decreasing ship speed, the sailing duration will be longer, as well as the required fuel consumption and cost (Schultz *et al.*, 2011; Hakim *et al.*, 2019). This phenomenon belongs to the category of energy waste, which can also increase the number of emissions into the air (Molland *et al.*, 2014). Moreover, the International Maritime Organization (IMO) is already worried about the level of air emissions from ships (IMO, 2009b; Smith *et al.*, 2014) by enforcing the Energy Efficiency Design Index (EEDI) (IMO, 2014) and the Ship Energy Efficiency Management Plan (SEEMP) regulations (IMO, 2009a). Additionally, the transmission of biofouling on a ship's hull from one water body to another can pose biosecurity threats and harm the local ecosystem (IMO, 2011; Ulman *et al.*, 2019).

Controlling the cleanliness of the ship's hull is one method of preventing the detrimental effects of biofouling (ICCT, 2011). To determine when a ship's hull should be cleaned by docking or underwater cleaning, one of the steps in controlling hull cleanliness is the early prediction of the effect of increased drag (Tian *et al.*, 2021; Dinariyana, Deva and Ariana, 2022; Degiuli *et al.*, 2023). Even this can be accomplished by investing in more sophisticated antifouling at an early stage (Yebra, Kiil and Dam-Johansen, 2004). The International Towing Tank Conference (ITTC) encourages researchers to investigate the impact of biofouling on ship resistance. The International Towing Tank Conference (ITTC) encourages researchers to investigate how biofouling affects ship resistance because biofouling has unique characteristics, such as non-uniform shape and non-homogeneous growth (ITTC, 2011). Differences have been noted the drag values caused by homogeneous and inhomogeneous biofouling (Suastika *et al.*, 2021; Song, Ravenna, *et al.*, 2021; Song, Demirel, *et al.*, 2021). There is still a great deal of ambiguity around predicting the increase in frictional resistance caused by roughness, such as a random roughness pattern and having many roughness parameters (Chung *et al.*, 2021). In fact, if the antifouling paint is too rough, it can increase the ship's resistance, so this factor should be considered (Schultz, 2007; Atencio and Chernoray, 2019; Hakim *et al.*, 2020; Utama *et al.*, 2021). "In addition, the roughness of biofouling also impacts the pressure resistance of the ship. (Song, Demirel and Atlar, 2019; Demirel, Turan and Incecik, 2017; Hakim, Maqbulyani, *et al.*, 2021; Regitasyali *et al.*, 2022).

The frictional resistance of a ship can be estimated by treating the hull as if it were shaped as a flat plate (Molland, Turnock and Hudson, 2017). The first systematic research was carried out by William Froude utilising flat plates tested on towing tanks around the 1860s. R. E. Froude, the son of William Froude, carried out the additional study and established a correlation between the frictional resistance and Reynolds number in 1888. Then, based on Von Karman's study findings, Schoenherr created an empirical formula in 1932 (Schoenherr, 1932), later adopted by the American Towing Tank Conference (ATTC) in 1947. Taking Hughes' equation into consideration, the International Towing Tank Conference (ITTC) adopted and modified the Schoenherr formula. The ITTC formula then becomes the norm for evaluating ship models as a forecast of power needs during the ship design process (ITTC, 2014).

The flat plate test is also the foundation for the prediction of the increase in frictional resistance caused by roughness. Townsin's prediction formula (Townsin, 2003) is equivalent to those created by Granville (1958) and (1987), where the ship's hull is assumed to be a flat plate. Based on the outcomes of wind tunnel tests with a flat surface (2D) model as well, Monty *et al.* (2016) expect an increase in frictional resistance caused by the roughness of tubeworm fouling. Using Computational Fluids Dynamics (CDF) simulation using a flat plate as their geometry model, Demirel, Turan and Incecik (2017) and Demirel *et al.* (2014) predicted an increase in frictional resistance taken on by the roughness of antifouling paints and biofouling. In addition, Demirel *et al.* (2017), Demirel *et al.* (2019), Utama *et al.* (2021), Farkas, Degiuli and Martić (2021), and Hakim, Suastika and Utama (2023) also predicted an increase in frictional resistance due to roughness by assuming that the ship's hull would be modelled as a flat plate.

Unfortunately, the real ships are not flat, meaning they have a form that affects ship's resistance. Different hull shapes of a ship result in different values of pressure resistance and wave resistance as well (Hakim *et al.*, 2023). However, if the ship's surface is rough due to biofouling, the changes in resistance values become interesting to study. The value of frictional drag along an object will differ depending on its shape (Currie, 2016). This difference is influenced by changing the flow velocity resulting from the shape of the object, which causes the pressure flow differences (Xia and Chen, 2016). A comparison of the frictional drag values along a flat plate (zero pressure gradient) and a non-flat object (non-zero pressure gradient) were conducted by Watmuff and Joubert (1983), Patel, Chen and Ju (1988), and Patel and Sarda (1990) for smooth conditions, and Speranza *et al.* (2019) for rough conditions. The curve plot shows different values between the flat plate and non-flat objects, and this also occurs for rough surfaces condition. However, Speranza *et al.* (2019) only compared one shape, which was the Wigley hull. However, the ship is built following a specific mission, allowing the hull's design or shape to be modified to suit the requirements. As a result, the hull will be longer or wider or fat or slim. As a result, the ship's hull includes parameters that naval architects frequently employ to do engineering analyses (Schneekluth and Bertram, 1998). The variables include the ratio of the ship's size, length to width (L/B), block coefficient (C_B), and center of buoyancy (L_{CB}), among others.

This paper will examine whether the hull's form parameters— L/B, C_B, and L_{CB}—have any manner of influence on the increased frictional resistance brought on by roughness. The method used is Computational Fluid Dynamics (CFD) simulation, combined with the Design of Experiment (DoE) to vary the models (Islam and Lye, 2009; Lye, 2002; Hakim, Nugroho, *et al.*, 2021). As an object research model, the Series 60 hull model was employed. A statistical technique called analysis of variance was performed to investigate the effect of the three parameters (L/B, C_B, and L_{CB}) on the magnitude of the increase in frictional resistance (ΔC_F) due to roughness.

2. MATERIAL AND METHOD

2.1. Model Geometry

The hull model utilised as object research in this study is the Series 60 ship's hull, which may be found in the Maxsurf software library. The Series 60 hull was created in the United States of America in the 1950s (Molland, Turnock and Hudson, 2017; Todd, 1953; Todd, Stuntz and Pien, 1957). Because it is one of the reference models and has a simpler shape, the Series 60 hull model was chosen because it is simple to transform. A transformation process is necessary to produce a hull model with the correct shape parameters. Figure 1 shows the Series 60 hull model created using the Maxsurf software.

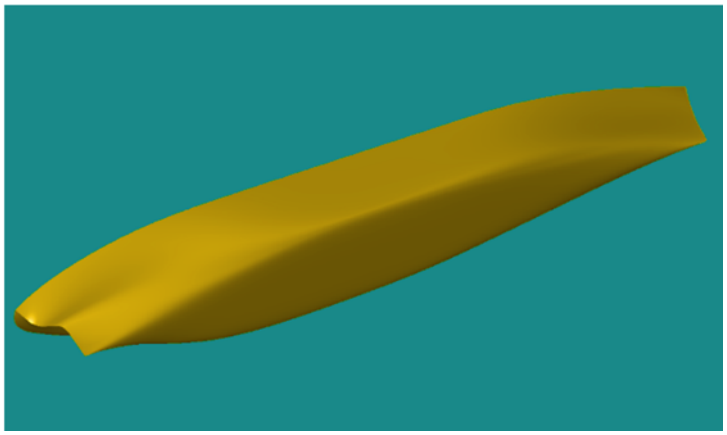

Figure 1. Isometric view of the Series 60 model (Bentley Systems, 2013).

This has been done with the aid of a tool called Parametric Transformation, which Maxsurf software has made available to change the shape of the hull. This tool can change the ship's hull to the desired form. By entering the necessary values, the hull can be altered as desired (Bentley Systems, 2013).

2.2. Model Variation

The three parameters chosen for this study's change of the hull form parameters are L/B (Length/Width), C_B (Block Coefficient), and L_{CB} (Length of center Buoyancy). The Design of Experiment (DOE) two fractional factorial design approach states that using three parameters, a total of 2^3 = 8 models must be simulated. Additionally, the lowest and highest values chosen and tabulated in Table 1 are used to determine the three parameters. The DOE combination matrix for each model is then shown in Table 2 for the eight models, each of which has a unique set of parameters.

The ship's length (L) is fixed at 100 m, its speed (V) is set at 10 m/s, and its surface roughness condition (k_s) at 3000 µm with a roughness constant (C_s) of 0.253 (Cebeci and Bradshaw, 1977). The hull roughness parameter is represented by k_s (equivalent sand-grain roughness height), which is equivalent to an average hull roughness of 5 mm surface length, R_{t50} 3000 µm (Schultz, 2007). Further in-depth explanations regarding k_s and C_s are available in the literature (Jimenez, 2004; Atencio and Chernoray, 2019; Andersson *et al.,* 2020; and Hakim, Suastika and Utama, 2023).

	Factor	Label	Low = -1	High = +1
a	Length/Breadth	L/B	5	10
b	Coefficient Block	C_B	0.65	0.75
c	Length of Center Buoyancy	L_{CB}	-2.5%	+2.5%

Table 1. The variation of parameters with their low (low) and high (high) values.

Combination	$X_{(L/B)}$	$X_{(C_B)}$	$X_{(L_{CB})}$	L/B	C_B	L_{CB}	Model label
0	-1	-1	-1	5	0.65	-2.5%	Model 1
a	+1	-1	-1	10	0.65	-2.5%	Model 2
b	-1	+1	-1	5	0.75	-2.5%	Model 3
c	-1	-1	+1	5	0.65	+2.5%	Model 4
ab	+1	+1	-1	10	0.75	-2.5%	Model 5
ac	+1	-1	+1	10	0.65	+2.5%	Model 6
bc	-1	+1	+1	5	0.75	+2.5%	Model 7
abc	+1	+1	+1	10	0.75	+2.5%	Model 8

Table 2. Two-level full factorial design matrix and data models.

Figure 2 and Figure 3 are examples of Series 60 hull lines plan models that have been transformed. Figure 2 is Model 1, which has an L/B ratio of 5, C_B of 0.65, and L_{CB} of -2.5%. Figure 3 is Model 4, which has an L/B ratio of 5, C_B of 0.65, and L_{CB} of +2.5%. From both figures, it can be seen that the centre of volume point is different, but it can be ensured that they have the same volume value.

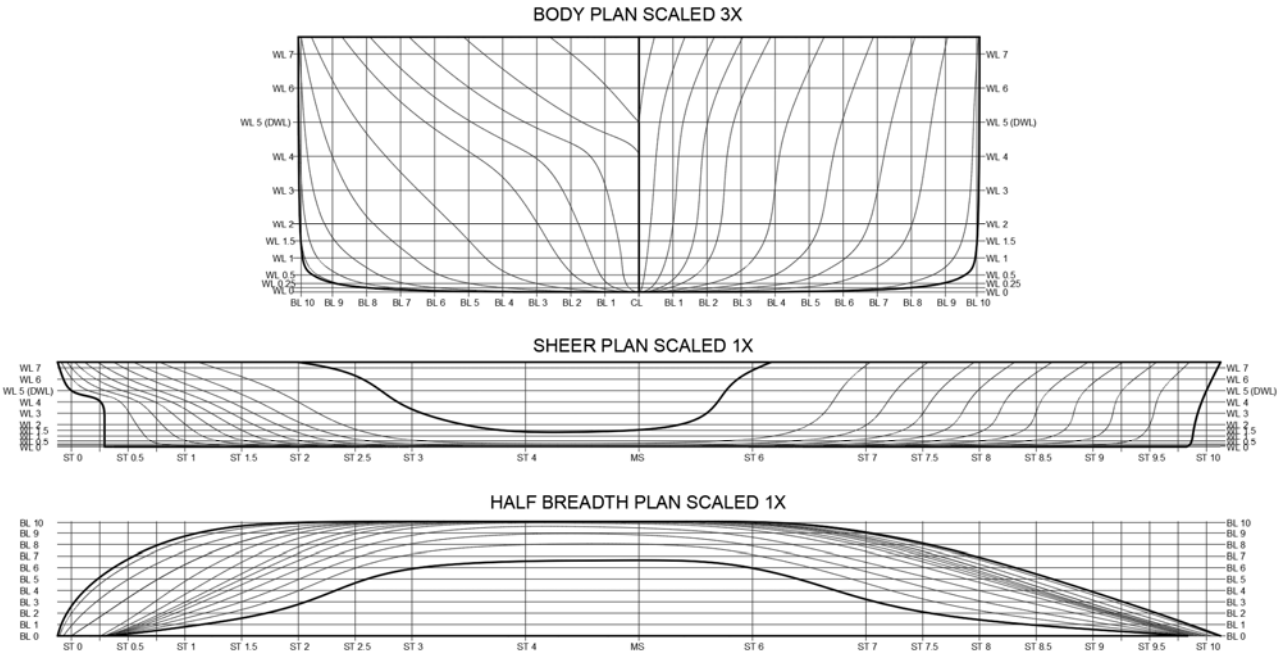

Figure 2. Lines Plan of Model 1.

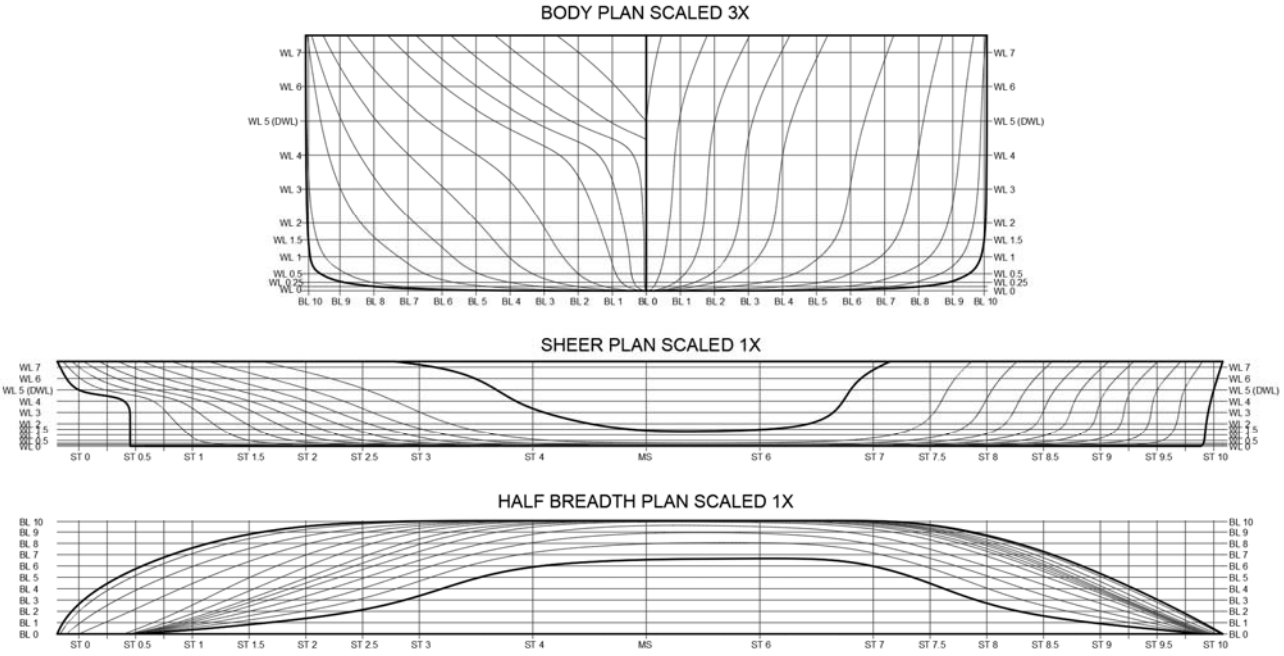

Figure 3. Lines Plan of Model 4.

2.3. Numerical modelling

2.3.1. Mathematical formulation

The equations in this study have been resolved by means of the steady RANS approach. The commercial CFD software ANSYS FLUENT solves the conservation of mass and momentum equations. Equations (1) and (2) provide the mean continuity and momentum equations for the incompressible flow. According to Equation (3), U_i is the average velocity component, $\bar{P}$ is the average pressure, ρ is the fluid's

density, μ is dynamic viscosity, u_i' is the fluctuation velocity component, $\rho\overline{U_i'U_j'}$ is the Reynolds stress, and $\overline{\tau_{ij}}$ is the tensor component of the average viscous stress (Ferziger and Perić, 2002). The solver uses the SIMPLE algorithm to discretise the equation governing, where the gradient occurs using the finite volume method. The second-order equations are used to discretise the continuity and momentum equations, and a residual of less than 10^{-4} is desired in the numerical calculations.

$$\frac{\partial(\rho\bar{U}_i)}{\partial x_i} = 0 \tag{1}$$

$$\frac{\partial(\rho\bar{U}_i)}{\partial t} + \frac{\partial}{\partial x_i}\left(\rho\bar{U}_i\bar{U}_j + \rho\overline{U_i'U_j'}\right) = -\frac{\partial\bar{P}}{\partial x_i} + \frac{\partial\overline{\tau_{ij}}}{\partial x_j} \tag{2}$$

$$\tau_{ij} = \mu\left(\frac{\partial\bar{U}_i}{\partial x_j} + \frac{\partial\bar{U}_j}{\partial x_i}\right) \tag{3}$$

Completing the RANS equation, the $k-\omega$ Shear Stress Transport (SST) turbulence model has been employed. The k-ε in the far field and the ω -model next to the wall are combined. Menter (1994) created the turbulence model, which consists of k as the turbulence kinetic energy and ω as the specific dissipation rate. The equation for kinetic energy is given in Equation (4), while the equation for the dissipation rate is given in Equation (5). The kinetic energy and momentum equations are discretised in the second order, and the residual for all numerical calculations is less than 10^{-4}.

$$\frac{D\rho k}{\mathrm{Dt}} = \tau_{ij}\frac{\partial U_i}{\partial \mathrm{x}_j} - \beta^*\rho\omega k + \frac{\partial}{\partial x_j}\left[(\mu + \sigma_k\mu_t)\frac{\partial k}{\partial \mathrm{x}_j}\right] \tag{4}$$

$$\frac{D\rho\omega}{\mathrm{Dt}} = \frac{\gamma}{v_t}\tau_{ij}\frac{\partial U_i}{\partial \mathrm{x}_j} - \beta\rho\omega^2 + \frac{\partial}{\partial x_j}\left[(\mu + \sigma_\omega\mu_t)\frac{\partial\omega}{\partial \mathrm{x}_j}\right] + 2\rho(1-F_1)\sigma_{\omega 2}\frac{1}{\omega}\frac{\partial k}{\partial x_j}\frac{\partial\omega}{\partial x_j} \tag{5}$$

2.3.2. Roughness Model with Wall Function approach

The hull roughness model employs a modified wall function method for this numerical simulation. This phenomenon was first revealed by Nikuradse (1933) and continued by Colebrook (1939). The roughness becomes a new velocity profile, exposing the mean velocity profile of the turbulence boundary layer structure for the smooth case (see Equation (6)) to a downward shift in the log law region (see Equation (7)), as seen in Figure 4 (Hama, 1954). In relation to the roughness Reynolds number ($k_s{}^+$), the shift value is known as the roughness function (ΔU^+) (Jimenez, 2004), see Equations (8) and (9). Where: U^+ is a non-dimensional average velocity profile equals U_y/U_τ; U_y is the average velocity at y (normal of the wall); U_τ is the frictional velocity defined as $\sqrt{\tau_w/\rho}$; τ_w is the magnitude of the shear stress and ρ is the density of the fluid; y^+ is the non-dimensional normal distance from the wall defined as yU_τ/ν; ν is the kinematic viscosity; κ is the von Karman constant, and B is the smooth-wall log law intercept; and k_s is the height of roughness.

$$U^+{}_{smooth} = \frac{1}{\kappa}\ln y^+ + B \tag{6}$$

$$U^+{}_{rough} = \frac{1}{\kappa}\ln y^+ + B - \Delta U^+ \tag{7}$$

$$\Delta U^+ = f\left(k_s{}^+\right) \tag{8}$$

$$k_s{}^{+} = \frac{k_s U_\tau}{\nu} \tag{9}$$

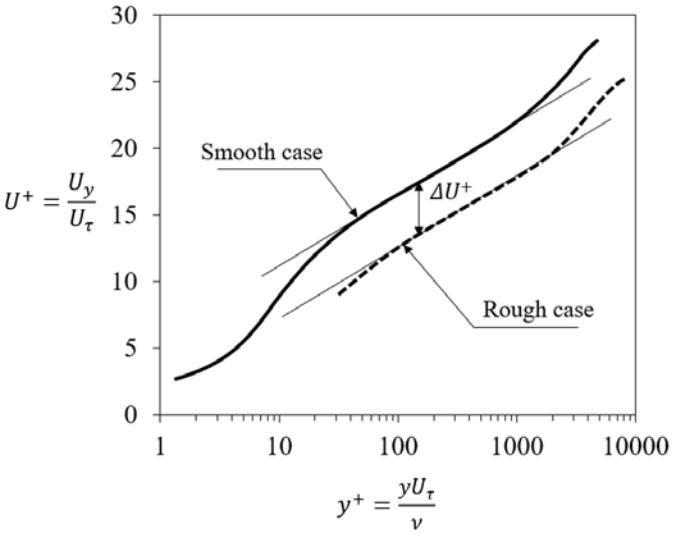

Figure 4. The roughness effect on the log-law velocity profile (Schultz and Flack, 2007).

The default roughness function code in the ANSYS FLUENT software was taken from Cebeci and Bradshaw (1977) and is based on Nikuradse data (Nikuradse, 1933). The roughness function, which has three phases—hydraulically smooth, transitional, and fully rough—is presented in Equation (10) (Andersson *et al.*, 2020), whereby k_s^+ is the Reynolds number of roughness, in the form $k_s U_\tau v^{-1}$; C_s is the roughness constant, taken as 0.253 following the Nikuradse curve (Atencio and Chernoray, 2019; Schultz and Flack, 2007); k_s is the roughness height which is equivalent to the grain roughness height.

$$\Delta U^+ = \begin{cases} 0 & \rightarrow k_s^+ \leq 2.25 \\ \frac{1}{\kappa}\ln\left[\frac{k_s^+ - 2.25}{87.75} + C_s k_s^+\right] \times \sin[0.426(\ln k_s^+ - 0.81)] & \rightarrow 2.25 < k_s^+ \leq 90 \\ \frac{1}{\kappa}\ln(1 + C_s k_s^+) & \rightarrow k_s^+ > 90 \end{cases} \tag{10}$$

2.3.3. Geometry and Boundary Conditions

In this simulation, the hull model is only used to represent the submerged portion of the water using the mono-fluid underwater approach. Figure 5 depicts the simulation's domain computation geometry. This model is only constructed halfway around the symmetry centreline to lessen the computational load. The domain's size is decided under certain circumstances. The section in front of the bow is assigned a length of $1L$, and the section behind the stern is assigned a length of $3L$. The section located $1L$ away from the centreline towards the side and $1L$ away from the draft towards the bottom is also included. The determination of this distance is based on an estimate of how to prevent the blockage effect from the wall. It is also ensured that the wall does not give a blocking effect because it is set as a free-slip boundary type.

In order for CFD simulation to produce accurate results, boundary conditions must be determined. Figure 5 can be used to describe the simulation's boundary conditions. It is decided to use a velocity inlet, where the free stream velocity determines the ship's speed. A pressure outlet with a hydrostatic setting was selected as the outlet to prevent any disturbance to the upstream propagation. The hull surface is given a no-slip or wall condition, and the values of k_s and C_s are input when the going is tough (as described in Equation (10)). Modelled as slip-free walls are the top, bottom, and sides (using symmetry or free-slip condition).

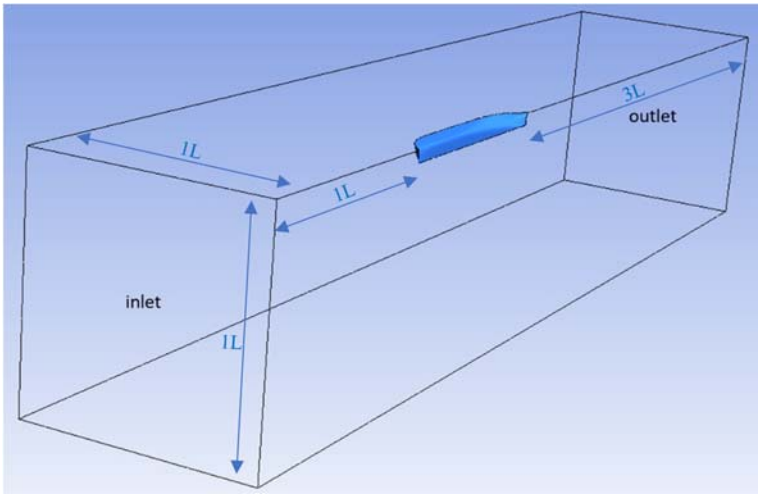

Figure 5. Domain and boundary conditions.

2.3.4. Mesh Generation

A mesh configuration with 1.7 million unstructured components and an expanding grid arrangement on the walls of a model ship with prism elements is shown in Figure 6. The value of y^+ near the best wall, which is set to 30< y^+ <300, requires the inflation layer method. For an accurate simulation, grid sensitivity testing must be performed on the quantity and configuration of these grids.

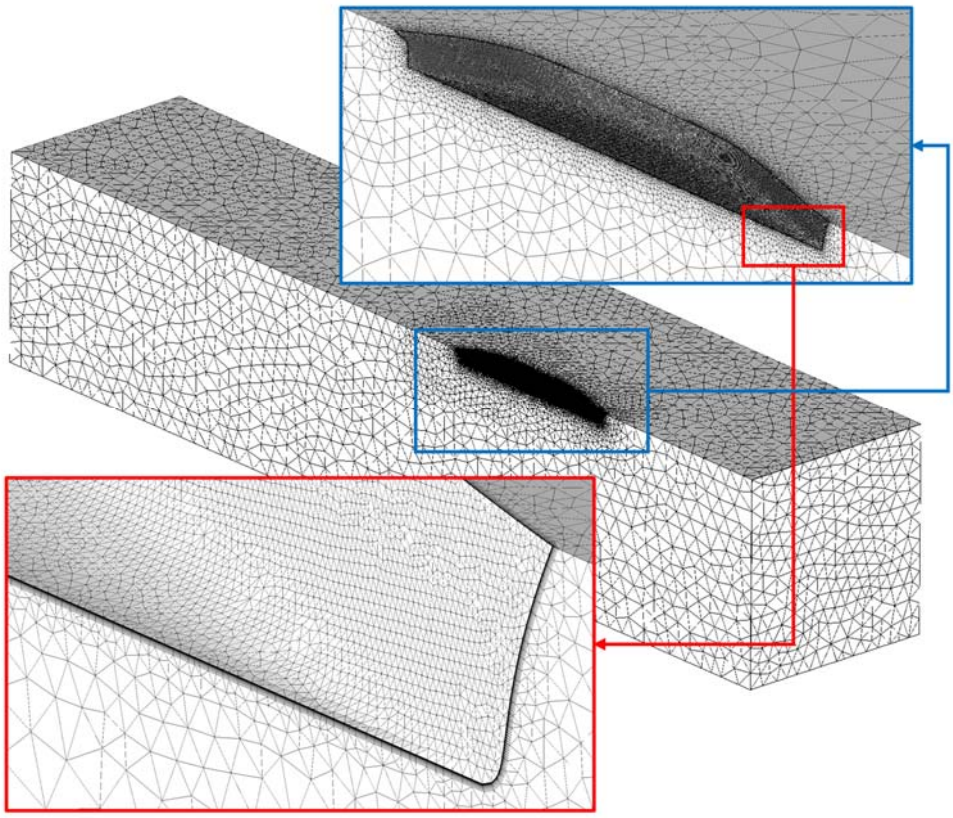

Figure 6. The appearance of mesh arrangement with the inflation layer for 1.7 million elements.

The center of the first cell above the wall's y^+ value must be bigger than the Reynolds local roughness value k_s^+ in order to accurately depict the roughness effect. If $y^+ < k_s^+$, ANSYS Fluent will virtually slide the wall

to guarantee that this requirement is always satisfied. The adjusted y^+ value for the centre of the first cell above the wall in the roughness situation considered in this study is provided as $y^+ = y^+ + k_s^+/2$. This value assumes a blockage effect of 50% of the roughness height. This approach can avoid singularity issues, and fine meshes can be correctly handled.

2.3.5. Verification Study

To evaluate the potential inaccuracies in both space and time of the simulations, convergence studies were conducted (ITTC, 2008). In order to estimate the numerical uncertainties, the Grid Convergence Index (GCI) method, based on Generalised Richardson Extrapolation (Richardson, 1911), has been employed. The GCI method involves calculating the ratio of the error between two different grid resolutions, which provides valuable information about the rate at which the error decreases as the resolution increases. According to Celik et al. (Celik *et al.*, 2008), the sequence of calculation for this method is as follows:

$$p_a = \frac{1}{\ln(r_{21})}\left|\ln\left|\frac{\varepsilon_{32}}{\varepsilon_{21}}\right| + q(p_a)\right| \tag{11}$$

$$q(p_a) = \ln\left(\frac{r_{21}^{p_a} - s}{r_{32}^{p_a} - s}\right) \tag{12}$$

$$s = \text{sign}\left(\frac{\varepsilon_{32}}{\varepsilon_{21}}\right) \tag{13}$$

Where, r_{21} and r_{32} are refinement factors given by $r_{21} = \sqrt[3]{N_1/N_2}$ for a spatial convergence study of a 3D model. convergence study. N_i are the cell number. $\varepsilon_{32} = \emptyset_3 - \emptyset_2$, $\varepsilon_{21} = \emptyset_2 - \emptyset_1$, and $\emptyset_i$ denotes the simulation result, i.e., R_T/Δ in this study.

The extrapolated value is calculated by:

$$\emptyset_{ext}^{21} = \frac{r_{21}^p \emptyset_1 - \emptyset_2}{r_{21}^p - 1} \tag{14}$$

The approximate relative error, e_a^{21}, is obtained by:

$$e_a^{21} = \left|\frac{\emptyset_1 - \emptyset_2}{\emptyset_1}\right| \tag{15}$$

The extrapolated relative error, e_{ext}^{21}, is obtained by:

$$e_{ext}^{21} = \left|\frac{\emptyset_{ext}^{21} - \emptyset_1}{\emptyset_{ext}^{21}}\right| \tag{16}$$

Finally, the fine-grid convergence index is found by

$$GCI_{fine}^{21} = \frac{1.25 e_a^{21}}{r_{21}^p - 1} \tag{17}$$

The result of numerical uncertainty calculation has been obtained as 1.07%, with the detailed calculation shown in Table 3.

N_1 (Coarse)	845,813	ε_{32}	-0.002
N_2 (Medium)	1,720,384	ε_{21}	-0.008
N_3 (Fine)	3,427,004	s	1.000
r_{21}	1.267	e_a^{21}	0.002
r_{32}	1.258	q	0.033
$\emptyset_1$	3.505	p_a	5.716
$\emptyset_2$	3.497	$\emptyset_{ext}^{21}$	3.535
$\emptyset_3$	3.495	e_{ext}^{21}	0.85%
		GCI_{fine}^{21}	1.07%

Table 3. Numerical uncertainty calculation results.

2.3.6. Validation Study

The simulation results have also been validated by contrasting them with empirical calculations to calculate the uncertainty of modelling (ITTC, 2008). For smooth settings, the empirical calculation is C_F ITTC 1957 (ITTC, 2014), and for simulated outcomes under rough conditions, Granville's (Granville, 1958) similarity law scaling approach is used. Equation (18) is used to determine the comparison of simulation results for smooth conditions by means of the C_F ITTC formula. Equation (19) is used to determine the comparison of simulation results for difficult settings with the Granville approach. In Table 4, the findings of all comparisons are compiled.

$$\mathrm{E}_{\mathrm{ITTC'57}}(\%) = \frac{C_{F_S} - C_{F\,(\mathrm{ITTC'57})}}{C_{F\,(\mathrm{ITTC'57})}} \times 100\% \tag{18}$$

$$\mathrm{E}_{\mathrm{Granville}}(\%) = \frac{C_{F_R} - C_{F\,(\mathrm{Granville})}}{C_{F\,(\mathrm{Granville})}} \times 100\% \tag{19}$$

The modelling uncertainty results under smooth conditions differ by -1.72% to 2.44%, according to C_F ITTC 1957, see Table 4, while the variations in the simulation result under rough conditions ranging from 0.07% to -4.07% according to Granville's similarity law scaling approach. These numbers need to be added to the error from the numerical uncertainty analysis from the verification study, namely $GCI_{3,2}$, which is 1.07%. The simulation results can be reviewed and considered valid based on the findings of these verification and validation calculations.

Model Label	C_{F_S} ×10^3	$\mathrm{E}_{\mathrm{ITTC'57}}$ (%)	C_{F_R}×10^3	$\mathrm{E}_{\mathrm{Granville}}$ (%)
Model 1	1.573	2.13	3.497	0.07
Model 2	1.514	-1.72	3.387	-3.08
Model 3	1.546	0.38	3.469	-0.73
Model 4	1.549	0.56	3.487	-0.23
Model 5	1.502	-2.44	3.374	-3.44
Model 6	1.508	-2.09	3.387	-3.07
Model 7	1.515	-1.61	3.393	-2.91
Model 8	1.541	0.04	3.352	-4.07

Table 4. Validation of simulation results against the empirical formulas.

3. RESULT AND DISCUSSION

3.1. The impact of roughness on frictional resistance

The ship model is only modelled in mono fluid throughout the CFD simulation that has been run in this scenario, which is a full viscous model. As a result, only pressure and frictional resistance—not wave resistance—were generated as resistance components. This approach was explicitly adopted because the analysis concentrates on the effects of frictional resistance.

In the wall function approach method, the wall shear stress value is obtained by projecting the slope value in the log-law region, as described in subsection 2.3.2. Due to the roughness condition represented by ΔU^+, the plot mean velocity profile shifts downwards, which means that the value of U^+ becomes lower as shown in Figure 7. As the value of U^+ becomes lower, according to the equation $U^+ = U_y/U_\tau$, with the value of U_y remaining constant, the value of U_τ increases. With the higher value of U_τ, the value of wall shear stress increases, as $\tau_w = \rho {U_\tau}^2$. The results of this simulation are shown in Figure 8, which describes the difference in shear stress values resulting from roughness modelling, where under rough conditions, the ship's frictional resistance becomes higher.

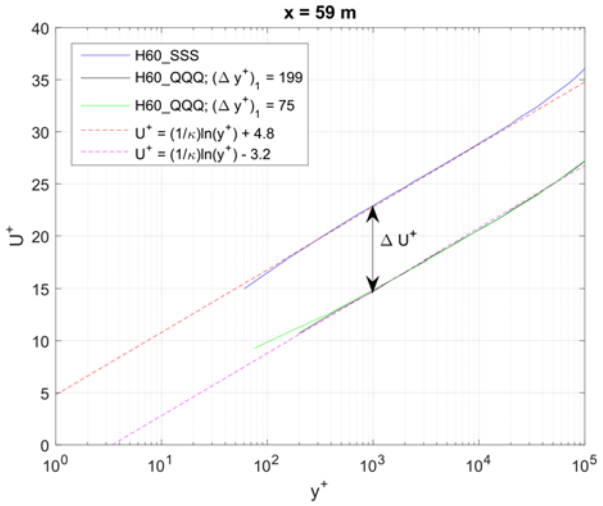

Figure 7. Example of mean velocity profile plot taken from Suastika *et al.* (2021) for smooth (top) and rough (bottom) conditions with wall function approach in CFD simulation.

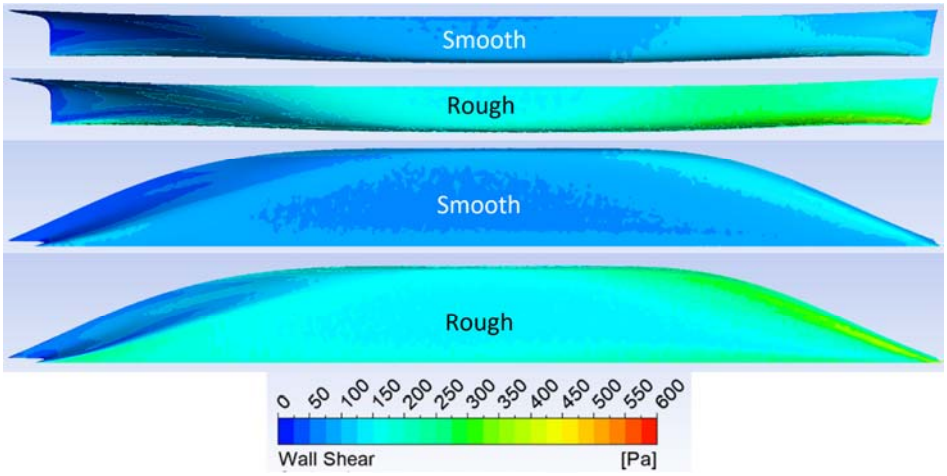

Figure 8. The difference in wall shear stress contour results between smooth and rough conditions in Model 4.

3.2. Local Frictional Resistance

In subsection 3.1 it is mentioned that roughness can cause an increase in U_τ and consequently result in an increase in shear stress τ_w or local friction drag. This section will analyse the shear stress values of various models representing differences in hull shape. Figure 9 to Figure 14 show the contour distribution of wall shear stress values influenced by the hull model form in 3D contour (Figure 9, Figure 11, and Figure 13) and waterline section (Figure 10, Figure 12, and Figure 14).

Figure 9 describes the shear stress contours of Models 7 and 8, which have different L/B values. From the results of the plot, it can be seen that the shear stress values do not differ much. In fact, it can be seen that the range of values remains the same. This reason is evidenced in Figure 10, which is a plot of the shear stress values at a 2.5 m waterline section, where the value of shear stress in rough conditions undergoes a fairly uniform increase from their smooth condition, extending from the front of the ship to the stern of the ship. As for the fluctuations themselves, the difference in L/B value does make the shear stress values different. Still, the value will be the same if the area under the curves is compared (integration value) from the front end to the back end. Model 8 has a higher shear stress value at the fore-end than Model 7. On the part approaching the shoulder of the ship's hull, the opposite occurs, where the shear stress value of Model 7 is higher than that of Model 8. Both models have the same shear stress in the parallel midship body. At the rear of the ship, the shear stress value for Model 8 is higher than that for Model 7. The same phenomenon can also be observed in hulls with differences in C_B values, as shown in Figure 11 and Figure 12, and in L_{CB} values, as shown in Figure 13 and Figure 14.

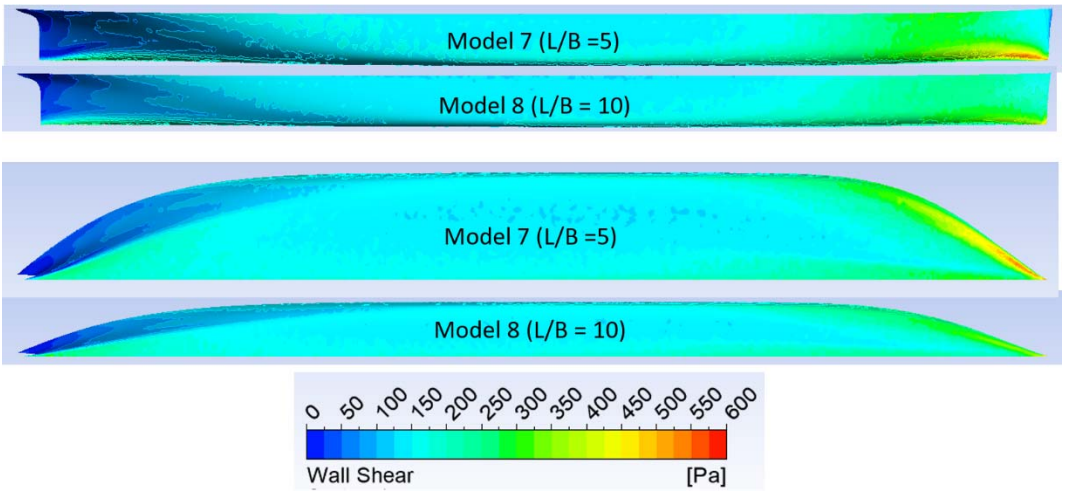

Figure 9. Wall shear stress contour of Models with different L/B values, where Model 7 (L/B = 5) and Model 8 (L/B =10).

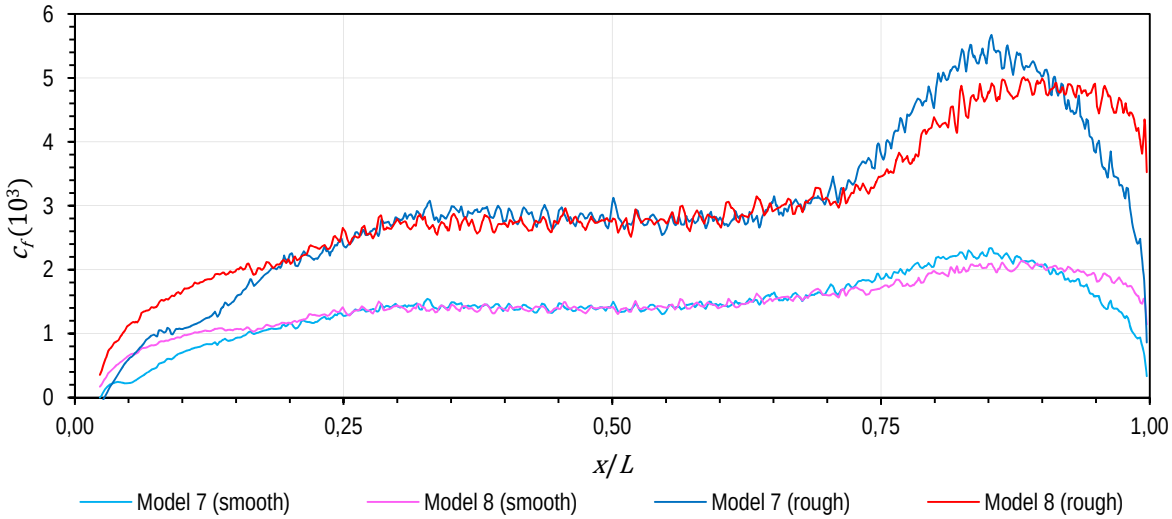

Figure 10. Plot of the local frictional coefficient at 2.5 m waterline of Models with different L/B values, where Model 7 (L/B = 5) and Model 8 (L/B =10).

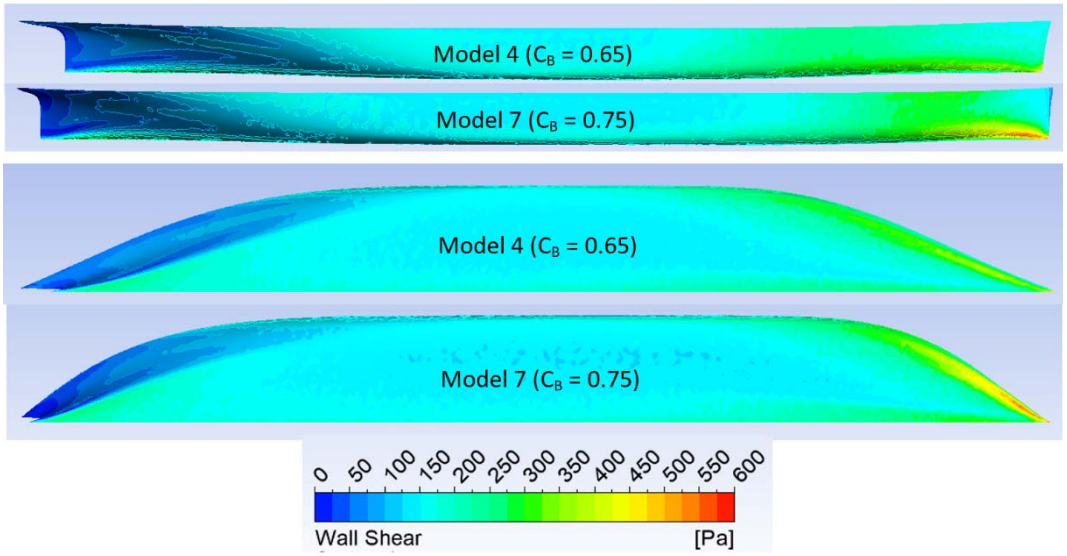

Figure 11. Wall shear stress contour of Models with different C_B values, where Model 4 (C_B = 0.65) and Model 7 (C_B = 0.75).

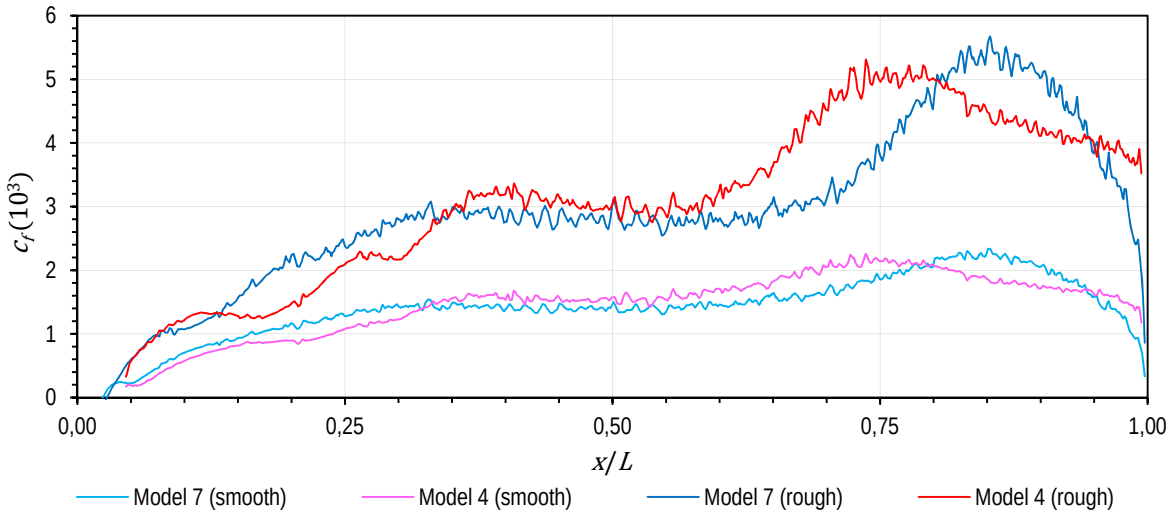

Figure 12. Plot of the local frictional coefficient at 2.5 m waterline of Models with different C_B values, where Model 7 (C_B = 0.75) and Model 4 (C_B = 0.65).

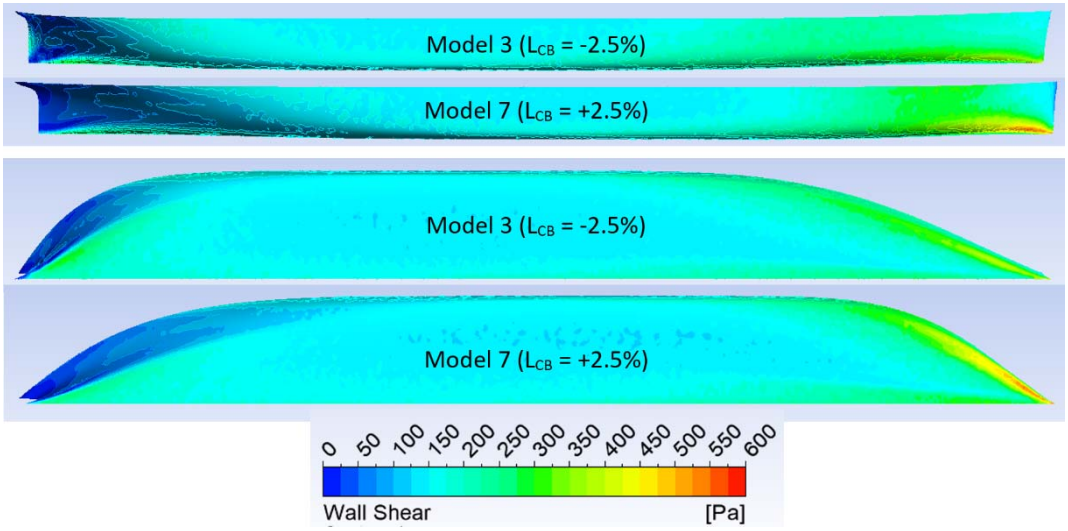

Figure 13. Wall shear stress contour of Models with different L_{CB} values, where Model 3 (L_{CB} = -2.5%) and Model 7 (L_{CB} = +0.25%).

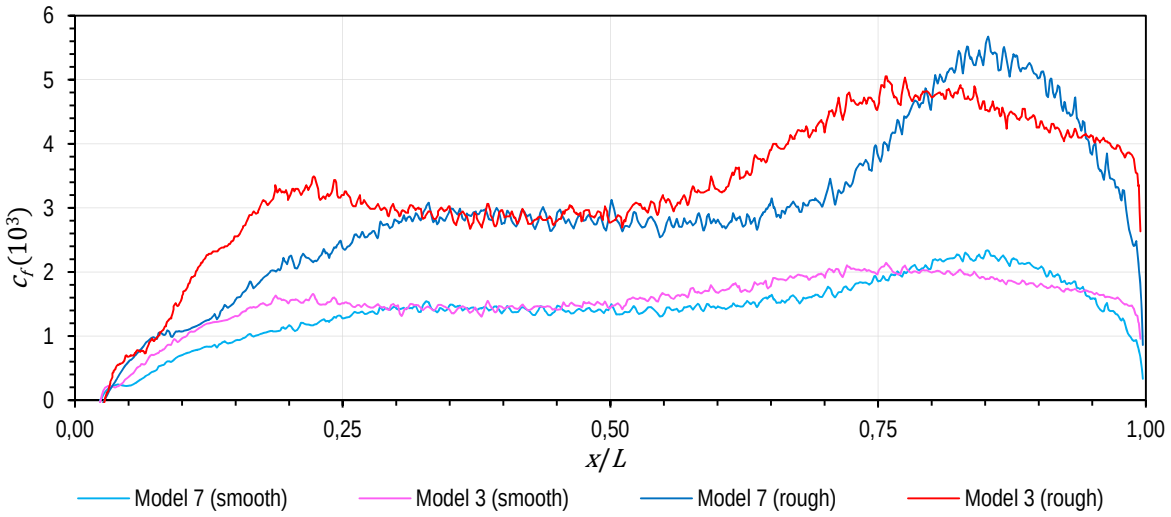

Figure 14. Plot of the local frictional coefficient at 2.5 m waterline Models with different L_{CB} values, where Model 7 (L_{CB} = +2.5%) and Model 3 (L_{CB} = -2.5%).

3.3. Overall Frictional Resistance

Equation (20) is used to determine the coefficient C_F, which represents frictional resistance. The other results in the form of pressure resistance, C_P, are computed based on Equation (21). In these equations, R_F is the total friction force that occurs in the hull model as the integration of local shear stress values (τ_w), R_P is the total pressure force that occurs in the hull model, ρ is the density of the fluid used, $U_\infty$is the velocity in the free stream, and A is the surface area of the hull model interacting with the fluid.

$$C_F = \frac{R_F}{\rho {U_\infty}^2 A/2} \tag{20}$$

$$C_P = \frac{R_P}{\rho {U_\infty}^2 A/2} \tag{21}$$

For rough conditions, it is calculated in the form of an increase in the coefficient of frictional resistance ΔC_F calculated based on Equations (22) and (24), where C_{F_R} is the coefficient of frictional resistance for rough conditions resulting from the CFD simulation. In addition to frictional resistance, the increase in pressure resistance due to roughness ΔC_P is also obtained from this simulation, where the calculation uses Equations (23) and (25), where C_{P_R} is the value of the pressure resistance coefficient for rough conditions. All calculation results from simulations for the eight models are tabulated in Table 5.

$$\Delta C_F = C_{F_R} - C_{F_S} \tag{22}$$

$$\Delta C_P = C_{P_R} - C_{P_S} \tag{23}$$

$$\Delta C_F\% = \frac{C_{F_R} - C_{F_S}}{C_{F_S}} \times 100\% \tag{24}$$

$$\Delta C_P\% = \frac{C_{P_R} - C_{P_S}}{C_{P_S}} \times 100\% \tag{25}$$

The values of C_{F_S}, C_{P_S}, ΔC_F, ΔC_P, $\Delta C_F\%$, $\Delta C_P\%$, and $\mathrm{E_{Granville}}\%$ have been subsequently examined to see if there had been any changes using analysis of variance. In order to determine if the three parameters (L/B, C_B, and L_{CB}) produce the same or distinct values, the calculation of the variance value tries to evaluate

how diverse the simulation results of the eight models are. In this manner, it is possible to determine whether or not the three parameters genuinely affect the result value.

1	2	3	4	5	6	7	8
Model label	C_{F_S} ×10^3	C_{P_S} ×10^3	ΔC_F ×10^3	ΔC_P ×10^3	ΔC_F%	ΔC_P%	$\mathrm{E}_{\mathrm{Granville}}$ (%)
Model 1	1.573	0.604	1.924	0.437	122.34	72.31	0.07
Model 2	1.514	0.237	1.873	0.093	123.77	39.28	-3.08
Model 3	1.546	1.365	1.923	0.609	124.42	44.63	-0.73
Model 4	1.549	0.517	1.938	0.287	125.14	55.54	-0.23
Model 5	1.502	0.377	1.872	0.190	124.59	50.44	-3.44
Model 6	1.508	0.215	1.879	0.078	124.64	36.23	-3.07
Model 7	1.515	0.740	1.878	0.391	123.91	52.90	-2.91
Model 8	1.541	0.308	1.812	0.106	117.59	34.41	-4.07
Variance (%)	1.57	27.73	2.10	31.59	1.96	17.24	1.62

Table 5. CFD simulation and variance analysis results.

From the analysis of variance values in Table 5, the lowest variance value is C_{F_S}, then sequentially from small to large, are $\mathrm{E}_{\mathrm{Granville}}(\%)$, $\Delta C_F\%$, ΔC_F, $\Delta C_P\%$, C_{P_S}, and ΔC_P. The values related to frictional resistance, namely C_{F_S}, ΔC_F, $\Delta C_F\%$, and $\mathrm{E}_{\mathrm{Granville}}(\%)$, have very small variance values, below 2.1%. When compared with the results related to pressure resistance, namely C_{P_S}, ΔC_P, dan $\Delta C_P\%$, it has a variance value from 17.24% to 31.59%.

These findings indicate that the L/B, C_B, and L_{CB} hull shape characteristics have no bearing on the increase in frictional resistance (ΔC_F), or that a flat plate can be used to forecast the increase in frictional resistance. The increase in pressure resistance (ΔC_P) brought on by roughness, as it turns out, varies depending on how these parameters are changed. Therefore, it may be claimed that the hull's shape affects the increase in pressure resistance brought on by roughness.

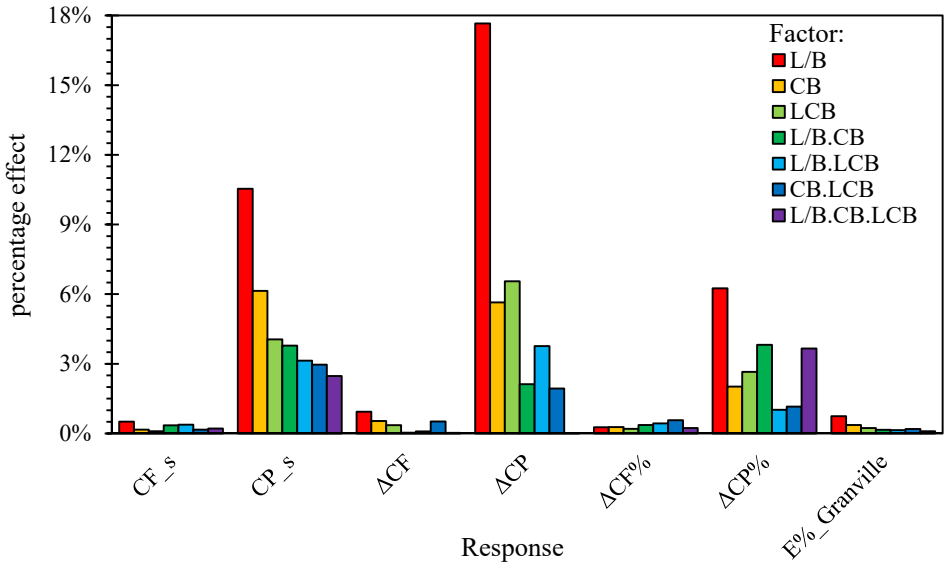

Figure 15. The percentage of each parameter and parameters' combinations' effects on the value of the response.

The percentage value of each factor's impact on the simulation outcomes or response and the interactions between factors is presented in Figure 15. The value effect is an output of the Design of Experiment (DOE) method, where the explanation can be seen in Hakim *et al.* (2021). According to the effect value analysis, all variables and their interactions have no bearing on any frictional resistance findings. However, these

parameters are very influential for all values related to pressure resistance, where these will be interesting as further research findings with more complex systematic variables.

4. CONCLUSION

The impact of the hull form factor represented by L/B, C_B, and L_{CB} on the magnitude of the increase in frictional resistance (ΔC_F) caused by roughness has been investigated using CFD simulation, as well as RANS-based CFD simulation with the SST $k-w$ turbulence model and a roughness model with the wall function approach. The CFD simulations have undergone verification and validation tests with acceptable results. The Series 60 hull model is employed and altered to produce the necessary variety. The Design of Experiment (DoE) method has determined the nature of the variation. Every simulation result is examined for variation analysis.

According to the analysis of variance values, the shape of the hull, as represented by the L/B, C_B, and L_{CB} parameters, has no significant effect on changes in the increase in frictional resistance (ΔC_F), regardless of whether the hull is modelled in smooth or rough conditions. Although differences in hull shape can cause variations in local shear stress values, the values are relatively similar when integrated into overall shear stress. These findings suggest that a flat plate assumption for the ship's hull can provide a convincing method for predicting the increase in frictional drag due to roughness.

Another finding from this research is that surface roughness can also increase pressure resistance. The increase in pressure resistance is also influenced by the hull shape parameters, which are believed to cause higher wake values at the stern of the hull due to the flow velocity being affected by surface roughness. Intensive parametric studies combining variations of hull shape parameters with surface roughness values are needed to further investigate these phenomena in future research.

ACKNOWLEDGEMENTS

This research project was supported by the hydrodynamic laboratory Department of Naval Architecture, Faculty of Engineering, Universitas Diponegoro, and Institut for Research and Community Services, Universitas Diponegoro. The author also appreciates the help of hydrodynamics laboratory, Department of Naval Architecture, Institut Teknologi Sepuluh Nopember, and the Hydrodynamics technology laboratory, National Research and Innovation Agency of Indonesia (BRIN).

REFERENCES

Andersson, J. et al., 2020. Review and comparison of methods to model ship hull roughness, *Applied Ocean Research*, 99, 102119. Available at: https://doi.org/10.1016/j.apor.2020.102119.

Atencio, B.N. and Chernoray, V., 2019. A resolved RANS CFD approach for drag characterization of antifouling paints, *Ocean Engineering*, 171, pp. 519–532. Available at: https://doi.org/10.1016/j.oceaneng.2018.11.022.

Bentley Systems, 2013. User Manual for Maxsurf Modeler.

Cebeci, T. and Bradshaw, P., 1977. Momentum transfer in boundary layers. New York: Hemisphere Publishing Corporation.

Celik, I.B. et al., 2008. Procedure for Estimation and Reporting of Uncertainty Due to Discretization in CFD Applications, Journal of Fluids Engineering, 130(7), 078001. Available at: https://doi.org/10.1115/1.2960953.

Chung, D. et al., 2021. Predicting the Drag of Rough Surfaces, Annual Review of Fluid Mechanics, 53(1), pp. 439–471. Available at: https://doi.org/10.1146/annurev-fluid-062520-115127.

Colebrook, C.F., 1939. Turbulent Flow in Pipes, with Particular Reference to the Transition Region Between the Smooth and Rough Pipe Laws, Journal of the Institution of Civil Engineers, 11(4), pp. 133–156. Available at: https://doi.org/10.1680/ijoti.1939.13150.

Currie, I.G., 2016. Fundamental Mechanics of Fluids. CRC Press. Available at: https://doi.org/10.1201/b12495.

Degiuli, N. et al., 2023. Optimization of Maintenance Schedule for Containerships Sailing in the Adriatic Sea, Journal of Marine Science and Engineering, 11(1), 201. Available at: https://doi.org/10.3390/jmse11010201.

Demirel, Y.K. et al., 2014. A CFD model for the frictional resistance prediction of antifouling coatings, Ocean Engineering, 89, pp. 21–31. Available at: https://doi.org/10.1016/j.oceaneng.2014.07.017.

Demirel, Y.K. et al., 2017. Effect of barnacle fouling on ship resistance and powering, Biofouling, 33(10), pp. 819–834. Available at: https://doi.org/10.1080/08927014.2017.1373279.

Demirel, Y.K. et al., 2019. Practical added resistance diagrams to predict fouling impact on ship performance, Ocean Engineering, 186, 106112. Available at: https://doi.org/10.1016/j.oceaneng.2019.106112.

Demirel, Y.K., Turan, O. and Incecik, A., 2017. Predicting the effect of biofouling on ship resistance using CFD, *Applied Ocean Research*, 62, pp. 100–118. Available at: https://doi.org/10.1016/j.apor.2016.12.003.

Dinariyana, A., Deva, P.P. and Ariana, I.M., 2022. Development of Model-Driven Decision Support System to Scheduling Underwater Hull Cleaning, Brodogradnja, 73(3), pp. 21–37. Available at: https://doi.org/10.21278/brod73302.

Farkas, A., Degiuli, N. and Martić, I., 2021. A novel method for the determination of frictional resistance coefficient for a plate with inhomogeneous roughness, Ocean Engineering, 237, 109628. Available at: https://doi.org/10.1016/j.oceaneng.2021.109628.

Ferziger, J.H. and Perić, M., 2002. Computational Methods for Fluid Dynamics, Computational Methods for Fluid Dynamics. Available at: https://doi.org/10.1007/978-3-642-56026-2.

Granville, P., 1958. The Frictional Resistance and Turbulent Boundary Layer of Rough Surfaces, Journal of Ship Research, 2(4), pp. 52–74.

Granville, P.S., 1987. Three Indirect Methods for the Drag Characterization of Arbitrarily Rough Surfaces on Flat Plates., Journal of Ship Research, 31(1), pp. 70–77.

Hakim, M.L. et al., 2017. Review of correlation between marine fouling and fuel consumption on ships, in SENTA: 17th Conference on Marine Technology. Surabaya, Indonesia, pp. II.122-129.

Hakim, M.L. et al., 2019. Investigation of fuel consumption on an operating ship due to biofouling growth and quality of anti-fouling coating, IOP Conference Series: Earth and Environmental Science, 339(1), pp. 012037. Available at: https://doi.org/10.1088/1755-1315/339/1/012037.

Hakim, M.L. et al., 2020. Drag Penalty Causing from the Roughness of Recently Cleaned and Painted Ship Hull Using RANS CFD, CFD Letters, 12(3), pp. 78–88. Available at: https://doi.org/10.37934/cfdl.12.3.7888.

Hakim, M.L., Nugroho, B., et al., 2021. Alternative Empirical Formula for Predicting the Frictional Drag Penalty due to Fouling on the Ship Hull using the Design of Experiments (DOE) Method, International Journal of Technology, 12(4), 829. Available at: https://doi.org/ 10.14716/ijtech.v12i4.4692.

Hakim, M.L., Maqbulyani, N., et al., 2021. Wind-Tunnel Experiments and CFD Simulations to Study the Increase in Ship Resistance Components due to Roughness, Journal of Sustainability Science and Management, 16(3), pp. 144–163. Available at: https://doi.org/10.46754/jssm.2021.04.012.

Hakim, M.L. et al., 2023. Investigating the Comparison of Ship Resistance Components between U and V-shaped Hulls, Jurnal Teknologi (Sciences & Engineering), 85(3), pp. 153–164. Available at: https://doi.org/10.11113/jurnalteknologi.v85.19382.

Hakim, M.L., Suastika, I.K. and Utama, I.K.A.P., 2023. A practical empirical formula for the calculation of ship added friction-resistance due to (bio)fouling, *O*cean Engineering, 271, 113744. Available at: https://doi.org/10.1016/j.oceaneng.2023.113744.

Hama, F., 1954. Boundary-layer characteristics for smooth and rough surfaces, Transactions - The Society of Naval Architects and Marine Engineers, 62, pp. 333–358.

ICCT, 2011. Reducing Greenhouse Gas Emissions from Ships, White Paper.

IMO, 2009a. Guidance for the Development of a Ship Energy Efficiency Management Plan (Seemp), The Marine Environment Protection Committee On Its Sixty-Third Session.

IMO, 2009b. Second IMO GHG study, 2009. International Maritime Organization (IMO), Maritime Organization (IMO) [Preprint].

IMO, 2011. MEPC.207(62) Guidelines for the control and management of ships' biofouling to minimize the transfer of invasive aquatic specie, Annex 26(July), pp. 1–25. Available at: http://www.imo.org/en/OurWork/Environment/Biofouling/Documents/RESOLUTION MEPC.207%5B62%5D.pdf.

IMO, 2014. Mepc.245(66) - 2014 Guidelines on the Method of Calculation of the Attained Energy Efficiency Design Index (EEDI) for New Ships, International Maritime Organization.

Islam, M.F. and Lye, L.M., 2009. Combined use of dimensional analysis and modern experimental design methodologies in hydrodynamics experiments, Ocean Engineering, 36, pp. 237–247. Available at: https://doi.org/10.1016/j.oceaneng.2008.11.004.

ITTC, 2008. Uncertainty Analysis in CFD Verification and Validation Methodology and Procedures, Recommended Procedures and Guidelines, 7.5-03-01.

ITTC, 2011. ITTC-Recommended Procedures and Guidelines: Practical Guidelines for Ship CFD Applications, 26th ITTC Specialist Committee on CFD in Marine Hydrodynamics.

ITTC, 2014. 1978 ITTC Performance Prediction Method, ITTC – Recommended Procedures and Guidelines, 7.5-02-03-(Rev. 3), p. Propulsion Committee of 27th ITTC.

Jimenez, J., 2004. Turbulent Flows Over Rough Walls, Annual Review of Fluid Mechanics, 36(1), pp. 173–196. Available at: https://doi.org/10.1146/annurev.fluid.36.050802.122103.

Lye, L.M., 2002. Design of experiments in civil engineering: Are we still in the 1920'S?, in Proceedings, Annual Conference - Canadian Society for Civil Engineering. Montreal, Canada.

Menter, F.R., 1994. Two-equation eddy-viscosity turbulence models for engineering applications, AIAA Journal, 32(8), pp. 1598–1605. Available at: https://doi.org/10.2514/3.12149.

Molland, A.F. et al., 2014. Reducing ship emissions: A review of potential practical improvements in the propulsive efficiency of future ships, Transactions of the Royal Institution of Naval Architects Part A: International Journal of Maritime Engineering, 156(PART A2), pp. 175–188. Available at: https://doi.org/10.3940/rina.ijme.2014.a2.289.

Molland, A.F., Turnock, S.R. and Hudson, D.A., 2017. Ship Resistance and Propulsion, Ship Resistance and Propulsion. Cambridge: Cambridge University Press. Available at: https://doi.org/10.1017/9781316494196.

Monty, J.P. et al., 2016. An assessment of the ship drag penalty arising from light calcareous tubeworm fouling, Biofouling, 32(4), pp. 451–464. Available at: https://doi.org/10.1080/08927014.2016.1148140.

Nikuradse, J., 1933. Laws of flow in rough pipes [English translation of Stromungsgesetze in rauhen Rohren], VDI-Forschungsheft 361. Beilage zu 'Forschung auf dem Gebiete des Ingenieurwesens' [Translation from NACA Technical Memorandum 1292] [Preprint]. Available at: https://doi.org/10.1063/1.1715007.

Patel, V.C., Chen, H.C. and Ju, S., 1988. Ship Stern and Wake Flows: Solutions of the FullyElliptic Reynolds-Averaged Navier-Stokes Equations and Comparisons with Experiments.

Patel, V.C. and Sarda, O.P., 1990. Mean-flow and turbulence measurements in the boundary layer and wake of a ship double model, Experiments in Fluids, 8, pp. 319–335.

Regitasyali, S. et al., 2022. Numerical investigation on the effect of homogenous roughness due to biofouling on ship friction resistance, IOP Conference Series: Earth and Environmental Science, 972(1), 012026. Available at: https://doi.org/10.1088/1755-1315/972/1/012026.

Richardson, L.F., 1911. The approximate arithmetical solution by finite differences of physical problems involving differential equations, with an application to the stresses in a masonry dam, Philosophical Transactions of the Royal Society A: Mathematical, Physical, and Engineering Sciences, 210(459–470), pp. 307–357. Available at: https://doi.org/10.1098/rsta.1911.0009.

Schneekluth, H. and Bertram, V., 1998. Ship Design for Efficiency and Economy. 2nd edn. Oxford: Butterworth-Heinemann.

Schoenherr, K.E., 1932. Resistance of flat surfaces, Trans SNAME, 40, pp. 279-313.

Schultz, M.P., 2007. Effects of coating roughness and biofouling on ship resistance and powering, Biofouling, 23(5), pp. 331–341. Available at: https://doi.org/10.1080/08927010701461974.

Schultz, M.P. et al., 2011. Economic impact of biofouling on a naval surface ship, Biofouling, 27(1), pp. 87–98. Available at: https://doi.org/10.1080/08927014.2010.542809.

Schultz, M.P. and Flack, K.A., 2007. The rough-wall turbulent boundary layer from the hydraulically smooth to the fully rough regime, Journal of Fluid Mechanics, 580, pp. 381–405. Available at: https://doi.org/10.1017/S0022112007005502.

Smith, T.W.P. et al., 2014. Third IMO GHG Study 2014, International Maritime Organization (IMO) London, UK. Available at: https://doi.org/10.1017/CBO9781107415324.004.

Song, S., Ravenna, R., et al., 2021. Experimental investigation on the effect of heterogeneous hull roughness on ship resistance, Ocean Engineering, 223. Available at: https://doi.org/10.1016/j.oceaneng.2021.108590.

Song, S., Demirel, Y.K., et al., 2021. Investigating the effect of heterogeneous hull roughness on ship resistance using CFD, Journal of Marine Science and Engineering, 9(2). Available at: https://doi.org/10.3390/jmse9020202.

Song, S., Demirel, Y.K. and Atlar, M., 2019. An investigation into the effect of biofouling on the ship hydrodynamic characteristics using CFD, Ocean Engineering, 175, pp. 122–137. Available at: https://doi.org/10.1016/j.oceaneng.2019.01.056.

Speranza, N. et al., 2019. Modelling of hull roughness, Ocean Engineering, 174, pp. 31–42. Available at: https://doi.org/10.1016/j.oceaneng.2019.01.033.

Suastika, I.K. et al., 2021. Characteristics of drag due to streamwise inhomogeneous roughness, Ocean Engineering, 223, p. 108632. Available at: https://doi.org/10.1016/j.oceaneng.2021.108632.

Tian, L. et al., 2021. Antifouling Technology Trends in Marine Environmental Protection, Journal of Bionic Engineering, 18(2), pp. 239–263. Available at: https://doi.org/10.1007/s42235-021-0017-z .

Todd, F.H., 1953. Some further experiments on single-screw merchant ship forms – Series 60,

Transactions of the Society of Naval Architects and Marine Engineers, 61, pp. 516–589.

Todd, F.H., Stuntz, G.R. and Pien, P.C., 1957. Series 60 – The effect upon resistance and power of variation in ship proportions, Transactions of the Society of Naval Architects and Marine Engineers, 65, pp. 445–589.

Townsin, R.L., 2003. The Ship Hull Fouling Penalty, Biofouling, 19(sup1), pp. 9–15. Available at: https://doi.org/10.1080/0892701031000088535.

Ulman, A. et al., 2019. Alien species spreading via biofouling on recreational vessels in the Mediterranean Sea, Journal of Applied Ecology. 56(12), pp. 2620–2629. Available at: https://doi.org/10.1111/1365-2664.13502.

Utama, I.K.A.P. et al., 2021. The effect of cleaning and repainting on the ship drag penalty, Biofouling, 37(4), pp. 372–386. Available at: https://doi.org/10.1080/08927014.2021.1914599.

Watmuff, J.H. and Joubert, P., 1983. Pressure Coefficient and Skin Friction Coefficient Distributions for the Wigley Hull.

Xia, C. and Chen, W., 2016. Boundary-layer transition prediction using a simplified correlation-based model, Chinese Journal of Aeronautics, 29(1), pp. 66–75. Available at: https://doi.org/10.1016/j.cja.2015.12.003.

Yebra, D.M., Kiil, S. and Dam-Johansen, K., 2004. Antifouling technology—past, present and future steps towards efficient and environmentally friendly antifouling coatings, Progress in Organic Coatings, 50(2), pp. 75–104. Available at: https://doi.org/10.1016/j.porgcoat.2003.06.001.